PERGAMON

International Journal of Solids and Structures 40 (2003) 5251–5270

INTERNATIONAL JOURNAL OF SOLIDS and STRUCTURES

www.elsevier.com/locate/ijsolstr

Effects of material gradients on transient dynamic mode-III stress intensity factors in a FGM

Ch. Zhang [a,*], J. Sladek [b], V. Sladek [b]

[a] *Department of Civil Engineering, University of Applied Sciences Zittau/Görlitz, Theodor-Koerner-Allee 16, D-02763 Zittau, Germany*

[b] *Institute of Construction and Architecture, Slovak Academy of Sciences, 84220 Bratislava, Slovakia*

Received 23 April 2003; received in revised form 24 April 2003

Abstract

This paper presents a transient dynamic crack analysis for a functionally graded material (FGM) by using a hypersingular time-domain boundary integral equation method. The spatial variations of the material parameters of the FGM are described by an exponential law. A numerical solution procedure is developed for solving the hypersingular time-domain traction BIE. To avoid the use of time-dependent Green's functions which are not available for general FGM, a convolution quadrature formula is adopted for approximating the temporal convolution, while a Galerkin method is applied for the spatial discretization of the hypersingular time-domain traction BIE. Numerical results for the transient dynamic stress intensity factors for a finite crack in an infinite and linear elastic FGM subjected to an impact anti-plane crack-face loading are presented and discussed. The effects of the material gradients of the FGM on the transient dynamic stress intensity factors and their dynamic overshoot over the corresponding static stress intensity factors are analyzed.
© 2003 Elsevier Ltd. All rights reserved.

Keywords: Functionally graded materials; Time-domain boundary integral equation method; Dynamic stress intensity factors; Dynamic overshoot; Dynamic fracture mechanics

1. Introduction

Functionally graded materials (FGM) received in recent years increasingly growing research interests in material sciences, applied mechanics and engineering sciences, due to their high performance and improved mechanical, thermal, corrosion-resistant and wear-resistant properties. The mechanical properties of FGM are non-homogeneous and changing continuously in position. FGM have no interfaces or interphases and are hence advantageous over the conventional composites and laminates. FGM can be applied to a wide range of engineering structures and components such as electronic devices, corrosion-resistant and

* Corresponding author. Tel.: +49-3583-611622; fax: +49-3583-611627.
E-mail address: c.zhang@hs-zigr.de (Ch. Zhang).
URL: http://www.hs-zigr.de/~zhang/.

0020-7683/$ - see front matter © 2003 Elsevier Ltd. All rights reserved.
doi:10.1016/S0020-7683(03)00243-9

wear-resistant coatings, optical films, thermal barrier coatings and biomaterials. The fracture and fatigue properties of FGM are important to their mechanical integrity, reliability and durability (Erdogan, 1995; Miyamoto et al., 1999) in practical engineering applications. Crack analysis of FGM provides a deep insight into the fracture and failure behaviors of FGM, which may aid in the design, optimization and applications of FGM. The corresponding analytical, numerical and experimental results have direct relevant applications in material sciences, fracture mechanics, non-destructive material testing, and engineering constructions.

Due to the non-homogeneous nature of FGM and the arising high mathematical complexities, only few investigations on transient dynamic responses of cracked FGM have been yet reported in literature. Steady state crack propagation analysis in FGM has been presented by Atkinson (1975), Atkinson and List (1978), Li and Weng (2002a), Meguid et al. (2002), Nakagaki et al. (1998), Parameswaran and Shukla (1999), and Wang and Meguid (1995). Dynamic responses of a crack in FGM under impact loading conditions have been investigated by Babaei and Lukasiwicz (1998), Li et al. (e.g., Li and Zou, 1999; Li et al., 1999, 2000, 2001a,b; Li and Weng, 2001, 2002b; Li et al., 2002), Marur and Tippur (2000), Nakagaki et al. (1995), Parameswaran and Shukla (1998), Rousseau and Tippur (2001a,b, 2002), Wang et al. (1998), and Zhang et al. (2001, 2003). Since analytical methods can be applied successfully only to very few simple dynamic crack problems in FGM, most of the afore mentioned works used either numerical or experimental methods. As numerical methods, the singular or the dual integral equation method in conjunction with the Laplace-transform technique, and the finite element method (FEM) are often used. An alternative method to the very established and widely applied FEM is the boundary element method (BEM) or boundary integral equation method (BIEM), which has been proven to be highly accurate and efficient for dynamic crack analysis of homogeneous and linear elastic materials (e.g., Aliabadi, 2002; Beskos, 1997; Domínguez, 1993; Zhang, 2002). In this paper, transient dynamic analysis of a finite anti-plane crack in a FGM subjected to an impact crack-face loading is presented by a using a time-domain BIEM.

In contrast to the BEM/BIEM for homogeneous and linear elastic materials, the applications of the BEM/BIEM to FGM are yet very limited, because the corresponding time-domain fundamental solutions or Green's functions for general FGM are either not available or mathematically too complex. A time-domain BIEM is presented and applied by Zhang et al. (2001, 2003) to a finite crack in an infinite FGM which is subjected to an impact anti-plane crack-face loading. To describe the spatial variations of the material parameters of the FGM, an exponential law is used where a symmetrical material gradation with respect to the crack-plane is assumed. In this paper, we extend the method of Zhang et al. (2001, 2003) to a more general case of FGM by removing the symmetry constraint in the material gradation with respect to the crack-plane. The initial-boundary value problem is formulated as a hypersingualr time-domain traction BIE. Since the corresponding time-domain Green's functions are not available for general FGM, the convolution quadrature formula of Lubich (1988) is applied for approximating the temporal convolution of the time-domain BIE. A spatial Galerkin method is adopted for the spatial discretization of the time-domain BIE. In lieu of the time-domain Green's functions which are frequently used in the conventional time-domain BEM/BIEM, the time-domain BIEM presented in this paper requires an explicit expression of the Laplace-domain Green's functions only, which can be expressed as Fourier integrals. A series of Chebyshev polynomials of second kind is applied for approximating the spatial variation of the unknown crack-opening-displacement (COD). An important advantage of the present time-domain BIEM is that it requires no special regularization or integration techniques for computing the arising hypersingular Hadamard finite-part integral. Numerical results are presented and discussed for the following three cases (see Fig. 1):

- *Case I:* Material gradient parallel to the crack-plane.
- *Case II:* Material gradient normal to the crack-plane.
- *Case III:* Material gradients parallel and normal to the crack-plane.

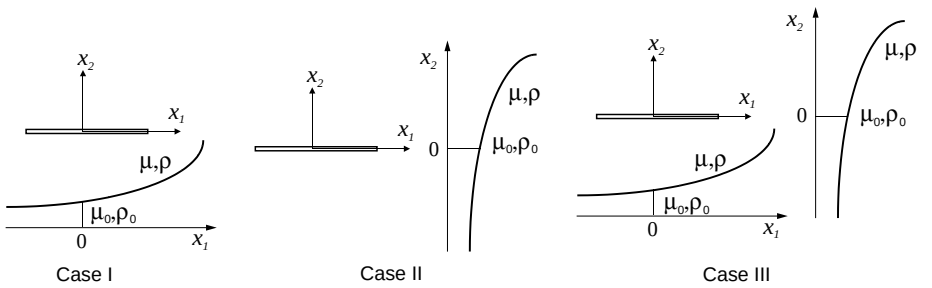

Fig. 1. Investigated cases—Case I: Material gradient parallel to the crack-plane, Case II: Material gradient normal to the crack-plane and Case III: Material gradients parallel and normal to the crack-plane.

Special attention of the analysis is devoted to the investigation of the effects of the material gradients on the transient dynamic stress intensity factors and their dynamic overshoot over the corresponding static stress intensity factors.

2. Problem formulation and time-domain BIE

Let us consider a finite crack of length $2a$ in an infinite and linear elastic FGM as shown in Fig. 2. The crack is subjected to an impact anti-plane crack-face loading, and the cracked FGM satisfies the equation of motion

$$\sigma_{3\alpha,\alpha} = \rho(\mathbf{x})\ddot{u}_3, \tag{1}$$

the Hooke's law

$$\sigma_{3\alpha} = \mu(\mathbf{x})u_{3,\alpha}, \tag{2}$$

the initial conditions

$$u_3(\mathbf{x},t) = \dot{u}_3(\mathbf{x},t) = 0, \quad t = 0, \tag{3}$$

and the traction boundary condition on the crack-faces

$$f_3(x_1, x_2 = 0, t) = \sigma^*_{32}(x_1,t) = \sigma^0_{32}H(t), \quad x_1 \in [-a,+a]. \tag{4}$$

In Eqs. (1)–(4), f_3 represents the traction component, u_3 denotes the displacement component in the x_3-direction, $\sigma_{3\alpha}$ are the shear stress components, $\mu(\mathbf{x})$ is the shear modulus, $\rho(\mathbf{x})$ is the mass density, σ^0_{32} is the stress amplitude, $H(t)$ is the Heaviside function, a comma after a quantity stands for partial derivatives with respect to spatial variables, superscript dots indicate temporal derivatives of the quantity, and the conventional summation rule over repeated indices is applied.

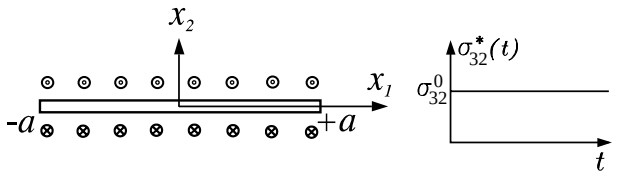

Fig. 2. A finite crack of length $2a$ in an infinite FGM.

To describe the spatial variations of the shear modulus and the mass density, the following exponential law has been used in the previous works (Zhang et al., 2001, 2003)

$$\mu(\mathbf{x}) = \mu_0 e^{\alpha x_1 + \beta|x_2|}, \qquad \rho(\mathbf{x}) = \rho_0 e^{\alpha x_1 + \beta|x_2| + \delta}, \tag{5}$$

which implies a symmetrical material gradient with respect to the crack-plane. Note here that the parameter δ in Eq. (5) is only a mathematical artifact and does not lead to any gradient effects. In this paper, the symmetry constraint and the parameter δ in Eq. (6) are removed. Thus, the shear modulus and the mass density are described by a general exponential law of the forms

$$\mu(\mathbf{x}) = \mu_0 e^{\alpha x_1 + \beta x_2}, \qquad \rho(\mathbf{x}) = \rho_0 e^{\alpha x_1 + \beta x_2}, \tag{6}$$

where μ_0, ρ_0, α and β are material parameters of the FGM. The exponential law (6) enables us to describe the spatial variations of the material constants in both unidirectionally and bidirectionally FGM.

The equation of motion (1) can be written in terms of the displacement component $u_3(\mathbf{x})$ as

$$\mu_{,1} u_{3,1} + \mu u_{3,11} + \mu_{,2} u_{3,2} + \mu u_{3,22} = \rho \ddot{u}_3. \tag{7}$$

By applying the one-sided Laplace transform

$$\hat{f}(p) = \int_0^\infty f(t) e^{-pt}\, dt \tag{8}$$

to Eq. (7), the equation of motion in the Laplace transformed domain takes the form

$$\mu_{,1} \hat{u}_{3,1} + \mu \hat{u}_{3,11} + \mu_{,2} \hat{u}_{3,2} + \mu \hat{u}_{3,22} = \rho p^2 \hat{u}_3, \tag{9}$$

where p is a complex Laplace transform parameter. The boundary and the continuity/discontinuity conditions on the crack-faces $|x_1| \leqslant a$ and the crack-plane $|x_1| \leqslant \infty$ can be stated as

$$\hat{\sigma}_{32}(x_1, 0) = \hat{\sigma}^*_{32}(x_1, 0), \quad |x_1| \leqslant a, \tag{10}$$

$$\hat{\sigma}_{32}(x_1, 0^+) = \hat{\sigma}_{32}(x_1, 0^-), \quad |x_1| \leqslant \infty, \tag{11}$$

$$\hat{u}_3(x_1, 0^+) = \hat{u}_3(x_1, 0^-), \quad |x_1| > a, \tag{12}$$

$$\hat{u}_3(x_1, 0^+) - \hat{u}_3(x_1, 0^-) = \Delta\hat{u}_3(x_1), \quad |x_1| < a, \tag{13}$$

where $\Delta\hat{u}_3(x_1)$ is the COD in the Laplace transformed domain.

The displacement component $\hat{u}_3(\mathbf{x})$ can be expressed as a Fourier integral of the form

$$\hat{u}_3(\mathbf{x}) = \begin{cases} \int_{-\infty}^{\infty} f_1(\xi) e^{i\xi x_1 - \gamma_1 x_2}\, d\xi, & x_2 > 0, \\ \int_{-\infty}^{\infty} f_2(\xi) e^{i\xi x_1 + \gamma_2 x_2}\, d\xi, & x_2 < 0, \end{cases} \tag{14}$$

where

$$\gamma_j = \frac{1}{2}\left\{ (-1)^{j-1}\beta + \sqrt{\beta^2 - 4[i\xi\alpha - \xi^2 - (\rho_0/\mu_0)p^2]} \right\}, \quad j = 1, 2. \tag{15}$$

In Eqs. (14) and (15), $f_1(\xi)$ and $f_2(\xi)$ are unknown functions to be determined, and the regularity condition at infinite requires $Re(\gamma_j) \geqslant 0$.

By substituting Eq. (14) into Hooke's law (2) and by using the continuity condition (11), a relation between f_1 and f_2 is obtained as

$$f_2 = -\frac{\gamma_1}{\gamma_2} f_1. \tag{16}$$

Eq. (14) together with Eqs. (12), (13) and (16) results in

$$\int_{-\infty}^{\infty} f_1(\xi)\frac{\gamma_1+\gamma_2}{\gamma_2}e^{i\xi x_1}\,d\xi = \begin{cases} 0, & |x_1| > a, \\ \Delta\hat{u}_3(x_1), & |x_1| < a. \end{cases} \tag{17}$$

Eq. (17) can be inverted as

$$f_1(\xi) = \frac{1}{2\pi}\frac{\gamma_2}{\gamma_1+\gamma_2}\int_{-a}^{+a} e^{-i\xi y_1}\Delta\hat{u}_3(y_1)\,dy_1. \tag{18}$$

Substitution of Eq. (18) into Eq. (16) yields

$$f_2(\xi) = -\frac{1}{2\pi}\frac{\gamma_1}{\gamma_1+\gamma_2}\int_{-a}^{+a} e^{-i\xi y_1}\Delta\hat{u}_3(y_1)\,dy_1. \tag{19}$$

By inserting Eqs. (18) and (19) into Eq. (14) a representation formula for the Laplace transform of the displacement component $\hat{u}_3(\mathbf{x})$ is obtained as

$$\hat{u}_3(\mathbf{x}) = \int_{-a}^{+a} \hat{\sigma}^{G}_{323}(\mathbf{x},\mathbf{y};p)\Delta\hat{u}_3(y_1)\,dy_1 \tag{20}$$

in which the Laplace transform of the dynamic stress Green's function $\hat{\sigma}^{G}_{323}(\mathbf{x},\mathbf{y};p)$ is given by

$$\begin{aligned} \hat{\sigma}^{G}_{323}(\mathbf{x},\mathbf{y};p) &= \frac{1}{2\pi}\int_{-\infty}^{\infty}\frac{\gamma_2}{\gamma_1+\gamma_2}e^{i\xi(x_1-y_1)-\gamma_1(x_2-y_2)}\,d\xi, \quad x_2 > y_2, \\ \hat{\sigma}^{G}_{323}(\mathbf{x},\mathbf{y};p) &= \frac{-1}{2\pi}\int_{-\infty}^{\infty}\frac{\gamma_1}{\gamma_1+\gamma_2}e^{i\xi(x_1-y_1)+\gamma_2(x_2-y_2)}\,d\xi, \quad x_2 < y_2. \end{aligned} \tag{21}$$

Substitution of Eq. (20) into Hooke's law (2) yields a representation integral for the Laplace transform of the traction component $\hat{f}_3(\mathbf{x})$

$$\hat{f}_3(\mathbf{x}) = \int_{-a}^{+a} \hat{T}^{G}_{323}(x_1,y_1;p)\Delta\hat{u}_3(y_1)\,dy_1, \tag{22}$$

where the Laplace-domain traction Green's function $\hat{T}^{G}_{323}(\mathbf{x},\mathbf{y};p)$ is given by

$$\begin{aligned} \hat{T}^{G}_{323}(\mathbf{x},\mathbf{y};p) &= \frac{\mu(\mathbf{x})}{2\pi}\int_{-\infty}^{\infty}\frac{\gamma_1\gamma_2}{\gamma_1+\gamma_2}e^{i\xi(x_1-y_1)-\gamma_1(x_2-y_2)}\,d\xi, \quad x_2 > y_2, \\ \hat{T}^{G}_{323}(\mathbf{x},\mathbf{y};p) &= \frac{\mu(\mathbf{x})}{2\pi}\int_{-\infty}^{\infty}\frac{\gamma_1\gamma_2}{\gamma_1+\gamma_2}e^{i\xi(x_1-y_1)+\gamma_2(x_2-y_2)}\,d\xi, \quad x_2 < y_2. \end{aligned} \tag{23}$$

In the time-domain, the corresponding representation formulae for the displacement and the traction components can be written as

$$u_3(\mathbf{x},t) = \int_{-a}^{+a} \sigma^{G}_{323}(\mathbf{x},\mathbf{y};t,\tau) * \Delta u_3(y_1,\tau)\,dy_1, \quad x_1 \notin [-a,+a], \tag{24}$$

$$f_3(\mathbf{x},t) = \int_{-a}^{+a} T^{G}_{323}(\mathbf{x},\mathbf{y};t,\tau) * \Delta u_3(y_1,\tau)\,dy_1, \quad x_1 \notin [-a,+a], \tag{25}$$

where an asterisk '*' denotes Riemann convolution which is defined by

$$f(t) = \int_0^t g(t-\tau)h(\tau)\,d\tau. \tag{26}$$

In Eqs. (24) and (25), $\sigma^{G}_{323}(\mathbf{x},\mathbf{y};t,\tau)$ and $T^{G}_{323}(\mathbf{x},\mathbf{y};t,\tau)$ are the corresponding time-domain stress and traction Green's functions, and $\Delta u_3(y_1,\tau)$ is the time-dependent COD defined by

$$\Delta u_3(y_1,\tau) = u_3(y_1,0^+,\tau) - u_3(y_1,0^-,\tau). \tag{27}$$

By taking the limit process $\mathbf{x} \to \Gamma_c^+ \in \{y_1 \leqslant |a|, y_2 = 0^+\}$ and using the boundary condition (4), a time-domain traction BIE is obtained as

$$\int_{-a}^{+a} T_{323}^{\mathrm{G}}(\mathbf{x},\mathbf{y};t,\tau) * \Delta u_3(y_1,\tau)\,\mathrm{d}y_1 = \sigma_{32}^*(x_1,t), \quad x_1 \in [-a,+a]. \tag{28}$$

By multiplying both sides of Eq. (28) with $\mu^{-1}(x_1,0)$ a more convenient form for the numerical solution of the time-domain BIE is obtained as

$$\mu^{-1}(x_1,0)\int_{-a}^{+a} T_{323}^{\mathrm{G}}(\mathbf{x},\mathbf{y};t,\tau) * \Delta u_3(y_1,\tau)\,\mathrm{d}y_1 = \sigma_{32}^*(x_1,t)\mu^{-1}(x_1,0), \quad x_1 \in [-a,+a]. \tag{29}$$

It can be easily shown that the traction BIE (29) has a hypersingularity of the order $1/|\mathbf{x}-\mathbf{y}|^2$ as $\mathbf{x} \to \mathbf{y}$. Here, the hypersingular integral is regarded as the Hadamard finite-part integral. To solve the hypersingular BIE (29), a spatial Galerkin method is applied, which requires no special integration or regularization technique for computing the arising hypersingular integral. It should be remarked here that an explicit expression of the time-domain traction Green's function $T_{323}^{\mathrm{G}}(\mathbf{x},\mathbf{y};t,\tau)$ is not needed in the present BIEM as will be seen in Section 3. In lieu of this, its Laplace transform $\widehat{T}_{323}^{\mathrm{G}}(\mathbf{x},\mathbf{y};p)$ is required, which is given by Eq. (23).

3. Numerical solution procedure

To solve the hypersingular time-domain BIE (29) and to avoid the use of the time-domain Green's functions which are not available for general FGM, the convolution quadrature formula of Lubich (1988) is applied for approximating the temporal convolution, while a Galerkin method is adopted for the spatial discretization of the hypersingular time-domain traction BIE. The unknown COD is approximated by the following Galerkin-ansatz

$$\Delta u_3(y_1,\tau) = \sqrt{a^2-y_1^2}\sum_{k=1}^{K} c_k(\tau) U_{k-1}\Big(\frac{y_1}{a}\Big), \tag{30}$$

where K is the total number of the used terms in the ansatz, $c_k(\tau)$ are the unknown time-dependent expansion coefficients and $U_{k-1}(y_1/a)$ are the Chebyshev polynomials of second kind. In Eq. (30), the term $\sqrt{a^2-y_1^2}$ is introduced to describe the local "square-root" behavior of the COD at the crack-tips $y_1 = \pm a$ correctly. Substituting Eq. (30) into Eq. (29), multiplying both sides by $\sqrt{a^2-x_1^2}U_{l-1}(x_1/a)$ and integrating them with respect to x_1 from $-a$ to $+a$, the following time-domain Galerkin-BIE is obtained

$$\begin{aligned}\sum_{k=1}^{K}\int_{-a}^{+a}\sqrt{a^2-x_1^2}U_{l-1}\Big(\frac{x_1}{a}\Big)\mu^{-1}(x_1,0)\int_{-a}^{+a}\sqrt{a^2-y_1^2}U_{k-1}\Big(\frac{y_1}{a}\Big)T_{323}^{\mathrm{G}}(x_1,y_1;t,\tau) * c_k(\tau)\,\mathrm{d}y_1\,\mathrm{d}x_1 \\ = \int_{-a}^{+a}\sigma_{32}^*(x_1,t)\mu^{-1}(x_1,0)\sqrt{a^2-x_1^2}U_{l-1}\Big(\frac{x_1}{a}\Big)\mathrm{d}x_1, \quad l = 1,2,\ldots,K.\end{aligned} \tag{31}$$

The application of the convolution quadrature formula of Lubich (1988)

$$f(t) = \int_0^t g(t-\tau)h(\tau)\,\mathrm{d}\tau \Rightarrow f(n\Delta t) = \sum_{j=0}^{n}\omega_{n-j}(\Delta t)h(j\Delta t) \tag{32}$$

to Eq. (31) results in a system of linear algebraic equations for the expansion coefficients as

$$\sum_{j=0}^{n}\sum_{k=1}^{K} A_{kl}^{n-j} c_k^j = f_l^n, \quad n = 0,1,2,\ldots,N, \tag{33}$$

where the time variable t is divided into N equal time-steps Δt. The time-domain system matrix and the right-hand side of Eq. (33) are given by

$$A_{kl}^n = \frac{r^{-n}}{M}\sum_{m=0}^{M-1} \hat{A}_{kl}(p_m)\mathrm{e}^{-2\pi \mathrm{i} nm/M}, \tag{34}$$

$$f_l^n = (-1)^l \int_{-a}^{+a} \sigma_{32}^*(x_1, n\Delta t)\mu^{-1}(x_1,0)\sqrt{a^2 - x_1^2}\, U_{l-1}\left(\frac{x_1}{a}\right)\mathrm{d}x_1 \tag{35}$$

in which (Lubich, 1988)

$$p_m = \delta(\zeta_m)/\Delta t, \quad \delta(\zeta_m) = \sum_{j=1}^{2}(1-\zeta_m)^j/j, \quad \zeta_m = r\mathrm{e}^{2\pi \mathrm{i} m/M}. \tag{36}$$

In this analysis, $M = N$ and $r^N = \sqrt{\epsilon}$ are chosen, and the error parameter in computing the Laplace-domain system matrix $\hat{A}_{kl}(p_m)$ is selected as $\varepsilon = 10^{-12}$. The time-domain system matrix in Eq. (33) corresponds to the integration weights $\omega_{n-j}(\Delta t)$ in the convolution quadrature formula (32). The time-domain system matrix defined by Eq. (34) can be computed very efficiently by using the fast Fourier transform (FFT). The Laplace-domain system matrix takes the following form

$$\hat{A}_{kl}(p) = (-1)^l \int_{-a}^{+a} \sqrt{a^2 - x_1^2}\, U_{l-1}\left(\frac{x_1}{a}\right)\mu^{-1}(x_1,0)\int_{-a}^{+a}\sqrt{a^2 - y_1^2}\, U_{k-1}\left(\frac{y_1}{a}\right)\widehat{T}_{323}^{\mathrm{G}}(x_1,y_1;p)\,\mathrm{d}y_1\,\mathrm{d}x_1. \tag{37}$$

where $\widehat{T}_{323}^{\mathrm{G}}(x_1,y_1;p)$ is the Laplace-domain traction Green's function. Substituting Eq. (23) into Eqs. (37) and (35), and using the following relations (Abramowitz and Stegun, 1972; Gradshteyn and Ryzhik, 1980)

$$\int_{-1}^{1} \mathrm{e}^{\mathrm{i}\alpha\eta}\sqrt{1-\eta^2}\, U_{k-1}(\eta)\,\mathrm{d}\eta = -\frac{k\pi}{\alpha}\mathrm{i}^{k+1}J_k(\alpha), \tag{38}$$

$$J_k(-\xi) = (-1)^k J_k(\xi), \qquad J_k(\mathrm{i}\xi) = \mathrm{i}^k I_k(\xi), \tag{39}$$

the Laplace-domain system matrix $\hat{A}_{kl}(p)$ and the right-hand side f_l^n can be evaluated as

$$\hat{A}_{kl}(p) = \frac{\pi}{2}\mathrm{i}^{k+l}kla^2\int_0^{\infty} F(\xi)\frac{1}{\xi^2}J_k(\xi a)J_l(\xi a)\,\mathrm{d}\xi, \tag{40}$$

$$f_l^n = -\frac{l}{\alpha}\pi a I_l(\alpha a)\sigma_{32}^0, \tag{41}$$

where $J_k(\cdot)$ is the Bessel function of first kind and kth order, $I_l(\cdot)$ is the modified Bessel function of first kind and lth order, and the function $F(\xi)$ is given by

$$F = \frac{\bar{\gamma}_1\bar{\gamma}_2}{\bar{\gamma}_1+\bar{\gamma}_2} + (-1)^{k+l}\frac{\gamma_1\gamma_2}{\gamma_1+\gamma_2}, \quad \bar{\gamma}_j(\xi) = \gamma_j(-\xi). \tag{42}$$

By using the following asymptotics (Abramowitz and Stegun, 1972)

$$J_k(\xi a) \propto \sqrt{\frac{2}{\pi(\xi a)}} \quad \text{as } |\xi a| \to \infty, \ |\xi a| \geqslant |k|, \tag{43}$$

$$F(\xi a) \propto C\xi + D \quad \text{as } |\xi a| \to \infty, \tag{44}$$

it can be shown that the integrand in Eq. (40) behaves as $1/(\xi a)^2$ which is not convenient for numerical integration due to its slow convergency. To achieve a fast convergency, the Laplace-domain system matrix $\hat{A}_{kl}(p)$ is recast into

$$\hat{A}_{kl}(p) = \frac{\pi}{2} \mathrm{i}^{k+l} kla^2 \left\{ \int_0^\infty \left[F(\xi) \frac{1}{\xi^2} - \frac{C}{\xi} - \frac{D}{\xi^2} \right] J_k(\xi a) J_l(\xi a) \, \mathrm{d}\xi + C\bar{I}_1 \right\}, \tag{45}$$

where use is made of the following integral relations (Gradshteyn and Ryzhik, 1980)

$$\bar{I}_1 = \int_0^\infty \frac{1}{\xi} J_k(\xi) J_l(\xi) \, \mathrm{d}\xi = \frac{\delta_{kl}}{k+l}, \tag{46}$$

$$\bar{I}_2 = \int_0^\infty \frac{1}{\xi^2} J_k(\xi) J_l(\xi) \, \mathrm{d}\xi = \begin{cases} 0, & k+l = \text{odd}, \\ \dfrac{4}{\pi} \dfrac{\mathrm{i}^{k-l+2}}{[(k+l)^2-1][(k-l)^2-1]}, & k+l = \text{even} \end{cases} \tag{47}$$

and the constants C and D are given by

$$C = \tfrac{1}{2}[1 + (-1)^{k+l}], \qquad D = \tfrac{1}{4}\mathrm{i}\alpha[1 - (-1)^{k+l}]. \tag{48}$$

The integrand in Eq. (45) behaves as $1/\xi^4$ for $\xi \to \infty$ and it can be integrated very efficiently by using the interval truncation method. A special feature of the present time-domain BIEM is that it uses Laplace-domain in lieu of time-domain Green's functions, which are frequently applied in the conventional time-domain BEM/BIEM. Furthermore, the present time-domain BIEM has two very attractive features: the arising Laplace-domain and time-domain system matrices $\hat{A}_{kl}(p)$ and A^n_{kl} are symmetric, and only a single spatial integral has to be computed numerically though the application of a spatial Galerkin method.

By taking the zero initial conditions (3) into account, an explicit time-stepping scheme from Eq. (33) is obtained as

$$c^n_k = \sum_{l=1}^{K} (A^0_{kl})^{-1} \left(f^n_l - \sum_{j=1}^{n-1} \sum_{i=1}^{K} A^{n-j}_{li} c^j_i \right), \quad n = 1, 2, \ldots, N, \tag{49}$$

in which $(A^0_{kl})^{-1}$ is the inverse matrix of A^0_{kl} at the time-step $n = 0$. The unknown time-dependent expansion coefficients c^j_k can be obtained numerically by using Eq. (49) time-step by time-step.

4. Numerical results and discussions

To check the accuracy and the efficiency of the present time-domain BIEM, extensive numerical tests have been carried out. Numerical results presented in the following have been obtained by using 20 terms in the Galerkin-ansatz, i.e., $K = L = 20$, and a time-step of $c_T \Delta t = a/20$ where $c_T = \sqrt{\mu_0/\rho_0}$. The stability of the present time-domain BIEM has been tested by several numerical examples. These tests have shown that the present time-domain BIEM is pretty insensitive to the chosen time-step $c_T \Delta t$, and it can provide stable numerical results even in the large-time range.

The asymptotic crack-tip field for linear elastic FGM has the same singularity and structure as for homogenous and linear elastic materials (Erdogan, 1995). Thus, the stress intensity factors can be also

applied to linear elastic FGM as crack-tip characterizing parameters. The transient dynamic stress intensity factors are related to the COD by

$$K_{\mathrm{III}}^{\pm}(t) = \frac{\sqrt{2\pi}}{4}\mu(\pm a, 0)\lim_{y_1 \to \pm a}\frac{1}{\sqrt{a \mp y_1}}\Delta u_3(y_1, t), \tag{50}$$

where $\pm$ indicates the crack-tips at $x_1 = \pm a$. Substituting Eq. (30) into Eq. (50) and using the identity (Abramowitz and Stegun, 1972)

$$U_k(\pm 1) = (\pm 1)^k(k+1), \tag{51}$$

a relation between the dynamic stress intensity factors and the expansion coefficients $c_k(t)$ is obtained as

$$K_{\mathrm{III}}^{\pm}(t) = \frac{\sqrt{\pi a}}{2}\mu(\pm a, 0)\sum_{k=1}^{K}(\pm 1)^{k-1}kc_k(t). \tag{52}$$

For convenience of the presentation, the transient dynamic stress intensity factors $\overline{K}_{\mathrm{III}}^{\pm}(t)$ are normalized as

$$\overline{K}_{\mathrm{III}}^{\pm}(t) = K_{\mathrm{III}}^{\pm}(t)/K_{\mathrm{III}}^{0}, \quad K_{\mathrm{III}}^{0} = \sigma_{32}^{0}\sqrt{\pi a}, \tag{53}$$

where σ_{32}^{0} represents the corresponding static crack-face loading.

4.1. Case I: material gradient parallel to the crack-plane

We first consider Case I in Fig. 1, which has also been investigated previously by Zhang et al. (2001, 2003). In this case, the shear modulus and the mass density change continuously parallel to the crack-plane. The variations of the shear modulus and the mass density are determined by an exponential law of the following forms

$$\mu(x_1) = \mu_0 \mathrm{e}^{\alpha x_1}, \qquad \rho(x_1) = \rho_0 \mathrm{e}^{\alpha x_1}. \tag{54}$$

Numerical results for the normalized dynamic stress intensity factors are presented in Fig. 3, versus the dimensionless time $c_{\mathrm{T}}t/a$. The special case $\alpha a = 0$ corresponds to a homogeneous material. Fig. 3 reveals that the material gradients have strong influences on the normalized dynamic stress intensity factors $\overline{K}_{\mathrm{III}}^{\pm}(t)$. The peak value and the static limit of the normalized dynamic stress intensity factor at the right crack-tip $\overline{K}_{\mathrm{III}}^{+}(t)$ increase, while those at the left crack-tip $\overline{K}_{\mathrm{III}}^{-}(t)$ decrease with increasing gradient parameter αa. The normalized dynamic stress intensity factors approach their corresponding static values at large-time $c_{\mathrm{T}}t/a$. Between the peak value and the static limit, the normalized dynamic stress intensity factor $\overline{K}_{\mathrm{III}}^{+}(t)$ at the right crack-tip may increase or decrease with increasing gradient parameter depending on the time instant considered, while $\overline{K}_{\mathrm{III}}^{-}(t)$ at the left crack-tip always decreases with increasing gradient parameter in the entire time-range under consideration.

For two different αa-values, the normalized dynamic stress intensity factors $\overline{K}_{\mathrm{III}}^{\pm}(t)$ are presented in Fig. 4, which shows that for $\alpha a \neq 0$ the right crack-tip in the direction of increasing shear modulus and mass density has a larger normalized dynamic stress intensity factor than the left crack-tip does, i.e., $\overline{K}_{\mathrm{III}}^{+}(t) \geqslant \overline{K}_{\mathrm{III}}^{-}(t)$. Compared to the dynamic stress intensity factors of a crack in a homogeneous material, the peak dynamic stress intensity factor $\overline{K}_{\mathrm{III}}^{+}(t)$ and its static limit at the right crack-tip in the direction of increasing shear modulus and mass density are amplified, which is unfavorable from the fracture mechanics point of view. In contrast, the peak dynamic stress intensity factor $\overline{K}_{\mathrm{III}}^{-}(t)$ and its static limit at the left crack-tip in the direction of decreasing shear modulus and mass density are reduced, which is favorable in view of the fracture mechanics analysis.

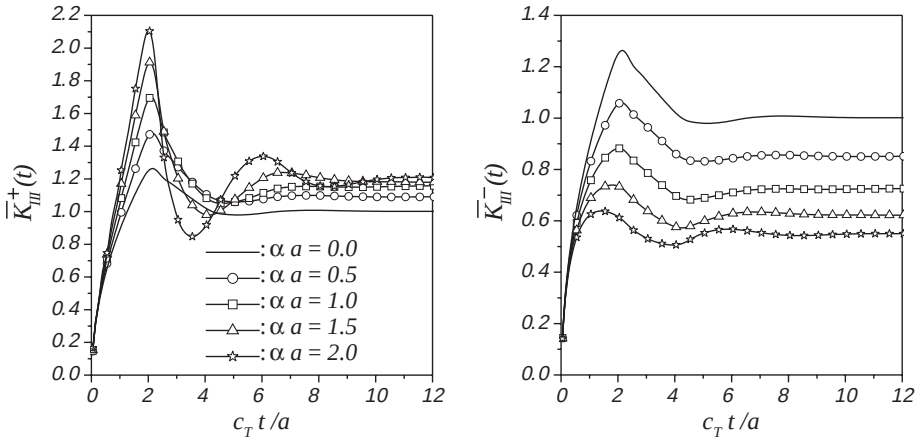

Fig. 3. Dynamic stress intensity factors for Case I.

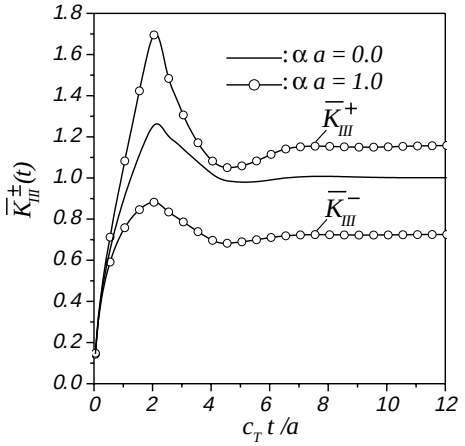

Fig. 4. A comparison of the dynamic stress intensity factors at both crack-tips for Case I ($\alpha a = 0.0$ and 1.0).

The dynamic overshoot of the stress intensity factors defined by

$$\text{Dynamic overshoot} = \frac{\max \overline{K}_{\mathrm{III}}^{\pm}(t) - \overline{K}_{\mathrm{III}}^{\pm(0)}}{\overline{K}_{\mathrm{III}}^{\pm(0)}} \tag{55}$$

is shown in Table 1 and Fig. 5, where $\overline{K}_{\mathrm{III}}^{\pm(0)}$ is the normalized static stress intensity factors given by

$$\overline{K}_{\mathrm{III}}^{\pm(0)} = K_{\mathrm{III}}^{\pm(0)}/K_{\mathrm{III}}^{0}, \quad K_{\mathrm{III}}^{0} = \sigma_{32}^{0}\sqrt{\pi a}. \tag{56}$$

Fig. 5 shows that in Case I the dynamic overshoot of the stress intensity factor at the right crack-tip increases while that at the left crack-tip decreases nearly linearly with increasing gradient parameter αa. Note here that the dynamic overshoot of the stress intensity factors for a homogeneous material (i.e., $\alpha a = 0.0$) predicted by the present time-domain BIEM is 26.14%, which is only 1.18% below the exact value $(4/\pi - 1) = 27.32\%$ (Thau and Lu, 1970). The normalized static stress intensity factor for a homogeneous

Table 1
Dynamic overshoot of the stress intensity factors for Case I

αa	$\max \overline{K}_{\mathrm{III}}^{+}$	$\overline{K}_{\mathrm{III}}^{+(0)}$	Overshoot	$\max \overline{K}_{\mathrm{III}}^{-}$	$\overline{K}_{\mathrm{III}}^{-(0)}$	Overshoot
0.0	1.2633	1.0015	26.14%	1.2633	1.0015	26.14%
0.5	1.4801	1.0929	35.43%	1.0599	0.8551	23.96%
1.0	1.6998	1.1479	48.08%	0.8822	0.7258	21.56%
1.5	1.9123	1.1808	61.95%	0.7393	0.6266	18.00%
2.0	2.1074	1.1966	76.12%	0.6383	0.5525	15.53%

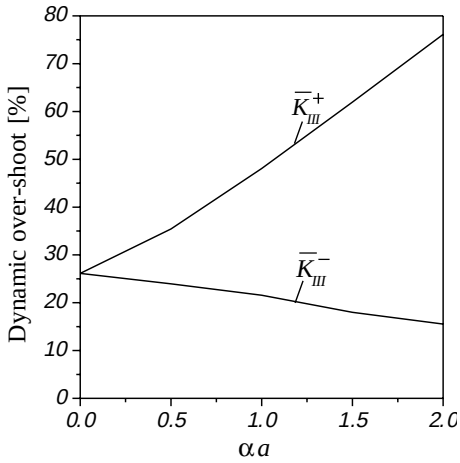

Fig. 5. Dynamic overshoot of the stress intensity factors for Case I.

material obtained by the present time-domain BIEM is 1.0015, which is only 0.15% higher than the exact value 1. This confirms the high accuracy of the time-domain BIEM applied in this paper.

4.2. Case II: material gradient normal to the crack-plane

In Case II as depicted in Fig. 1, the shear modulus and the mass density vary continuously in the direction normal to the crack-plane, which are described by an exponential law of the forms

$$\mu(x_2) = \mu_0 \mathrm{e}^{\beta x_2}, \qquad \rho(x_2) = \rho_0 \mathrm{e}^{\beta x_2}. \tag{57}$$

Fig. 6 shows the corresponding numerical results for the normalized dynamic stress intensity factor as a function of the dimensionless time $c_{\mathrm{T}}t/a$. The special case of a homogeneous material is recovered by setting $\beta a = 0$. Due to the symmetry of the problem it holds $\overline{K}_{\mathrm{III}}^{+} = \overline{K}_{\mathrm{III}}^{-}$. The peak value of the normalized dynamic stress intensity factors increases with increasing gradient parameter βa which is unfavorable. As the material gradient parameter βa increases, more pronounced oscillations in the normalized dynamic stress intensity factors are observed. In contrast to the dynamic stress intensity factors for a finite crack in a homogeneous material with $\beta a = 0.0$, additional local peak values of the transient dynamic stress intensity factors with slowly decreasing amplitudes are noted in the cases of $\beta a = 1.5$ and 2.0. After their peak values, the normalized dynamic stress intensity factors $\overline{K}_{\mathrm{III}}^{\pm}$ show a complicated dependence on the gradient parameter βa and the normalized time $c_{\mathrm{T}}t/a$.

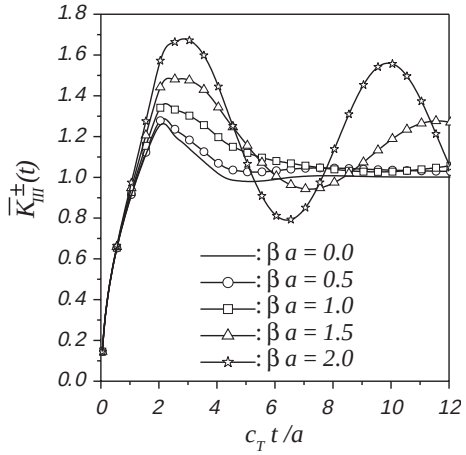

Fig. 6. Dynamic stress intensity factors for Case II.

Table 2
Dynamic overshoot of the stress intensity factors for Case II

βa	$\max \overline{K}_{\mathrm{III}}^{\pm}$	$\overline{K}_{\mathrm{III}}^{\pm(0)}$	Overshoot
0.0	1.2633	1.0015	26.14%
0.5	1.2874	1.0280	25.23%
1.0	1.3615	1.0762	26.51%
1.5	1.4858	1.1308	31.39%
2.0	1.6791	1.1875	41.40%

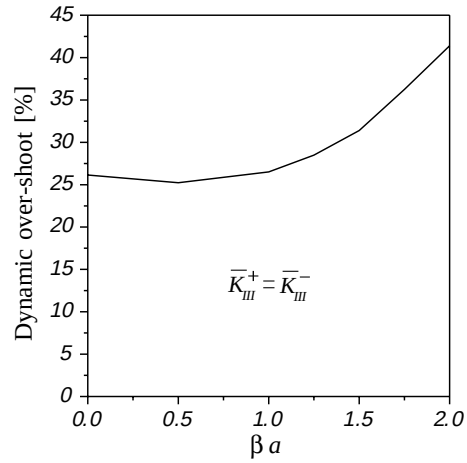

Fig. 7. Dynamic overshoot of the stress intensity factors for Case II.

Table 2 and Fig. 7 show the dynamic overshoot of the stress intensity factors for Case II, versus the gradient parameter βa. For small gradient parameter, say $\beta a < 1.0$, the dynamic overshoot of the stress

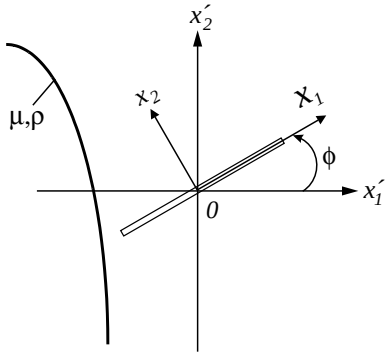

Fig. 8. Arbitrary crack orientation in a FGM with a unidirectional gradation.

intensity factors remains nearly constant, while it increases with increasing gradient parameter βa for large values of βa. It should be noted here that the normalized dynamic stress intensity factors for large gradient parameter βa oscillate about a constant value and no static value in the large-time limit can be attained by using the present time-domain BIEM. In this case, the average of the maximum and the minimum dynamic stress intensity factors in the large-time range is taken as the static values. For a fixed gradient parameter, the maximum dynamic overshoot of the stress intensity factors in Case II is smaller than in Case I.

4.3. Case III: material gradients parallel and normal to the crack-plane

In Case III of Fig. 1, the material is functionally graded in two directions. The spatial variations of the shear modulus and the mass density are described by the exponential law (6). Since two gradient parameters are needed here, the situation becomes very tangled. Here we consider a simple case where the material gradation is unidirectional but the crack has an arbitrary orientation with respect to the material gradient (see Fig. 8). This enables us to consider the effects of the material gradient and the crack orientation separately. In the material coordinate system $x_1' - x_2'$, the shear modulus and the mass density are determined by

$$\mu(x_2') = \mu_0 \mathrm{e}^{\beta' x_2'}, \qquad \rho(x_2') = \rho_0 \mathrm{e}^{\beta' x_2'}. \tag{58}$$

By using the following relation for the coordinate transform

$$\begin{Bmatrix} x_1' \\ x_2' \end{Bmatrix} = \begin{bmatrix} \cos\phi & -\sin\phi \\ \sin\phi & \cos\phi \end{bmatrix} \begin{Bmatrix} x_1 \\ x_2 \end{Bmatrix}, \tag{59}$$

we obtain the material constants in the crack coordinate system $x_1 - x_2$

$$\mu(x_1, x_2) = \mu_0 \mathrm{e}^{\beta' \sin\phi x_1 + \beta' \cos\phi x_2}, \qquad \rho(x_1, x_2) = \rho_0 \mathrm{e}^{\beta' \sin\phi x_1 + \beta' \cos\phi x_2}, \tag{60}$$

where ϕ represents the inclination angle of the crack. A comparison of Eq. (60) with Eq. (6) yields the following relation between the gradient parameters and the crack orientation angle

$$\alpha = \beta' \sin\phi, \qquad \beta = \beta' \cos\phi \tag{61}$$

or equivalently

$$\beta' = \sqrt{\alpha^2 + \beta^2}, \qquad \phi = \tan^{-1}\left(\frac{\alpha}{\beta}\right). \tag{62}$$

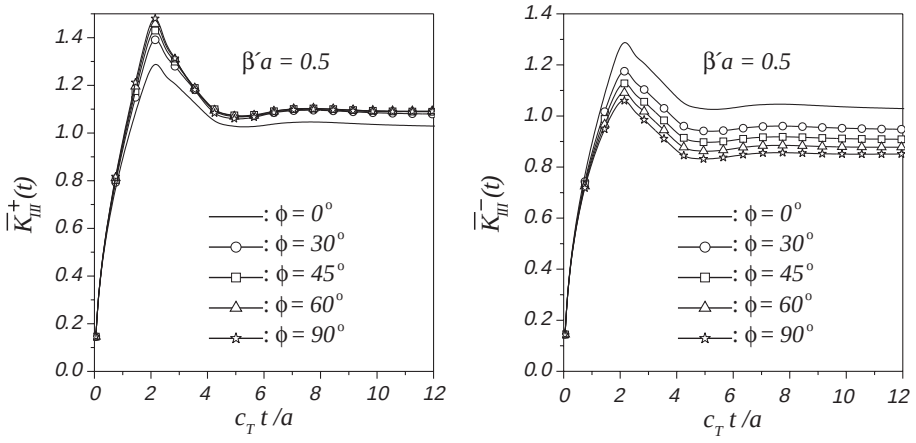

Fig. 9. Dynamic stress intensity factors for Case III ($\beta' a = 0.5$, ϕ in degrees).

Note here that the two special cases considered previously, i.e., Cases I and II, can be obtained by setting the inclination angles $\phi = 90°$ and $0°$ in Eq. (60).

For two different values of the gradient parameter $\beta' a = 0.5$ and 1.0 and for several values of the inclination angle ϕ, numerical results for the normalized dynamic stress intensity factors are presented in Figs. 9 and 10 versus the dimensionless time $c_T t/a$. The corresponding gradient parameters αa and βa in the $x_1 - x_2$-system are given in Table 3. Figs. 9 and 10 show that the crack orientation with respect to the material gradient may have significant influences on the transient dynamic stress intensity factors. For a fixed gradient parameter $\beta' a$, the peak dynamic stress intensity factor at the crack-tip $x_1 = +a$ increases with increasing inclination angle ϕ, while the opposite is observed for the normalized dynamic stress intensity factor at the crack-tip $x_1 = -a$. Surprisingly, the static limit of the normalized dynamic stress intensity factor at the crack-tip $x_1 = +a$ is less sensitive to the gradient parameter $\beta' a$ than that at the crack-tip $x_1 = -a$. For $\beta' a = 1.0$ and after the peak has been reached, the normalized dynamic stress intensity factor $\overline{K}_{\mathrm{III}}^{+}$ at $x_1 = +a$ may decrease with increasing orientation angle ϕ.

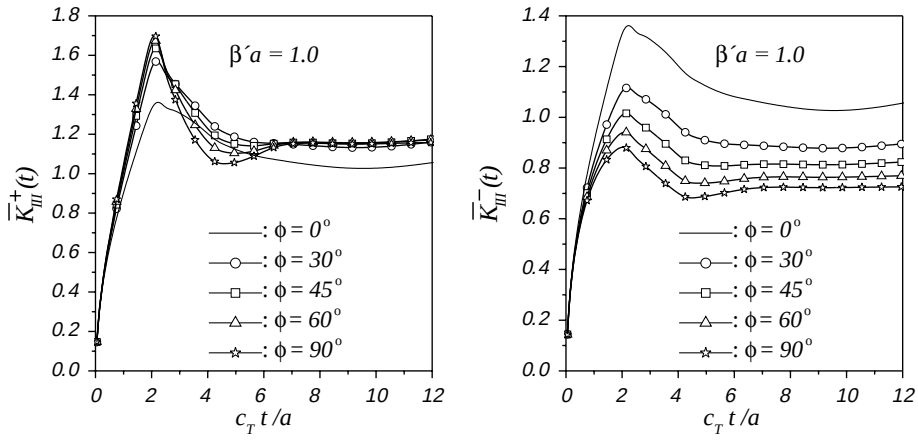

Fig. 10. Dynamic stress intensity factors for Case III ($\beta' a = 1.0$, ϕ in degrees).

Table 3
Gradient parameters for Case III ($\beta' a = 0.5$ and 1.0)

$\beta' a = 0.5$	αa	βa	$\beta' a = 1.0$	αa	βa
$\phi = 0°$	0.0	0.5	$\phi = 0°$	0.0	1.0
$\phi = 30°$	0.25	0.433	$\phi = 30°$	0.5	0.866
$\phi = 45°$	0.354	0.354	$\phi = 45°$	0.707	0.707
$\phi = 60°$	0.433	0.25	$\phi = 60°$	0.866	0.5
$\phi = 90°$	0.5	0.0	$\phi = 90°$	1.0	0.0

To compare the dynamic stress intensity factors at both crack-tips more clearly, numerical results for $\phi = 45°$, $\beta' a = 0$ and $\beta' a = 1$ are presented in Fig. 11. As in Case I, the normalized dynamic stress intensity factor at the crack-tip $x_1 = +a$ in the direction of increasing shear modulus and mass density is larger than that at the crack-tip $x_1 = -a$, i.e., $\overline{K}^{+}_{\mathrm{III}}(t) \geqslant \overline{K}^{-}_{\mathrm{III}}(t)$. In comparison with the transient dynamic stress intensity factors for a crack in a homogeneous material (i.e., $\beta' a = 0.0$), the normalized dynamic stress intensity factor $\overline{K}^{+}_{\mathrm{III}}(t)$ at the crack-tip $x_1 = +a$ in the direction of increasing shear modulus and mass density is increased, while the dynamic stress intensity factor $\overline{K}^{-}_{\mathrm{III}}(t)$ at the crack-tip $x_1 = -a$ in the direction of decreasing shear modulus and mass density is reduced.

For two values of the gradient parameter $\beta' a = 0.5$ and 1.0, the dynamic overshoot of the stress intensity factors is given in Table 4 and Fig. 12, versus the crack orientation angle ϕ. From these results it can be concluded that the dynamic overshoot of the stress intensity factor at the crack-tip in the direction of increasing material constants increases while that at the crack-tip in the direction of decreasing material parameters decreases more or less monotonically with increasing crack orientation angle ϕ. A maximum dynamic overshoot is obtained at the crack-orientation angle $\phi = 90°$, i.e., Case I when the material gradient is parallel to the crack-plane.

To explore the effects of the gradient parameter $\beta' a$ on the normalized dynamic stress intensity factors for an inclined crack orientation with respect to the material gradient, numerical results are presented in Figs. 13 and 14 for two selected values of the inclination angle $\phi = 30°$ and 60°. The corresponding gradient parameters in the $x_1 - x_2$-system are given in Table 5. Figs. 13 and 14 show some combined effects of parallel (Case I) and perpendicular (Case II) crack orientations as presented in Figs. 3 and 6. For small or moderate gradient parameter $\beta' a$, $\overline{K}^{+}_{\mathrm{III}}(t)$ at the crack-tip $x_1 = +a$ increases while $\overline{K}^{-}_{\mathrm{III}}(t)$ at the crack-tip

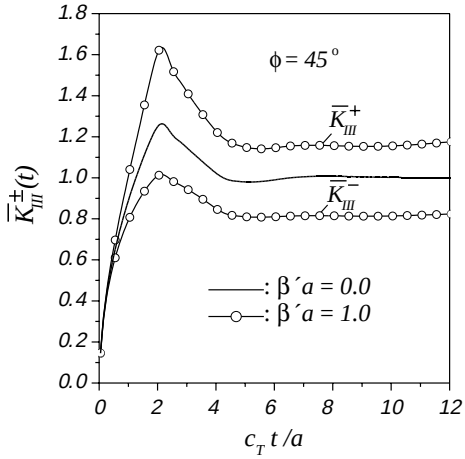

Fig. 11. A comparison of the dynamic stress intensity factors at both crack-tips for Case III ($\phi = 45°$).

Table 4
Dynamic overshoot of the stress intensity factors for $\beta' a = 0.5$ and $\beta' a = 1.0$

$\beta' a = 0.5$	Overshoot K_{III}^{+}	Overshoot K_{III}^{-}	$\beta' a = 1.0$	Overshoot K_{III}^{+}	Overshoot K_{III}^{-}
$\phi = 0°$	25.23%	25.23%	$\phi = 0°$	26.51%	26.51%
$\phi = 30°$	28.94%	23.86%	$\phi = 30°$	34.05%	23.48%
$\phi = 45°$	31.27%	23.78%	$\phi = 45°$	39.04%	22.72%
$\phi = 60°$	33.39%	23.84%	$\phi = 60°$	43.60%	22.12%
$\phi = 90°$	35.43%	23.96%	$\phi = 90°$	48.08%	21.56%

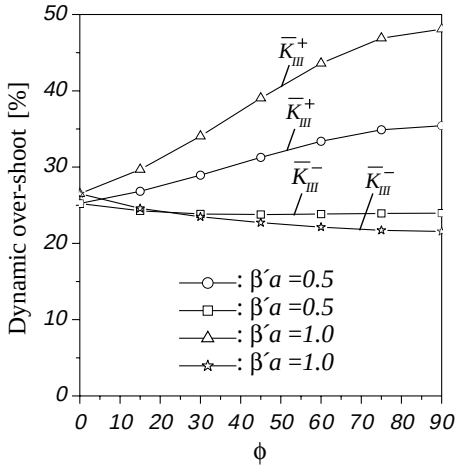

Fig. 12. Dynamic overshoot of the stress intensity factors for Case III ($\beta' a = 0.5$ and 1.0, ϕ in degrees).

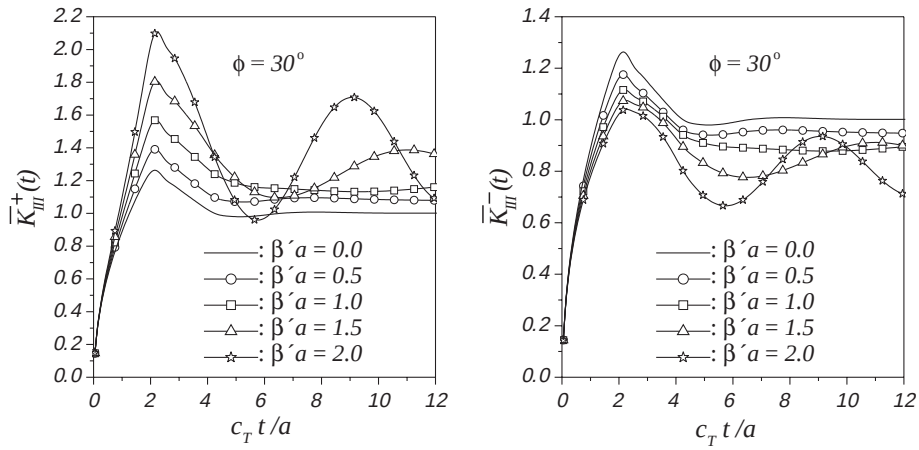

Fig. 13. Dynamic stress intensity factors for Case III ($\phi = 30°$).

$x_1 = -a$ decreases with increasing gradient parameter $\beta' a$. Furthermore, the normalized dynamic stress intensity factors approach in this case their corresponding static values very quickly. On the other hand,

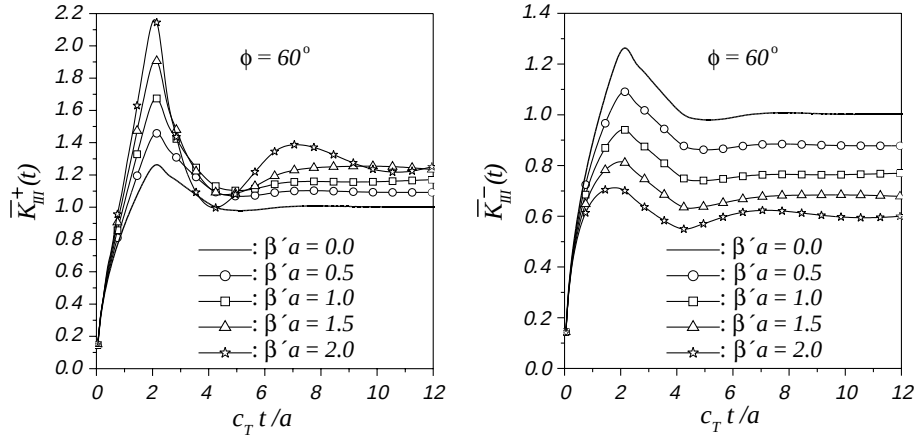

Fig. 14. Dynamic stress intensity factors for Case III ($\phi = 60°$).

Table 5
Gradient parameters for Case III ($\phi = 30°$ and 60°)

$\phi = 30°$	αa	βa	$\phi = 60°$	αa	βa
$\beta' a = 0.0$	0.0	0.0	$\beta' a = 0.0$	0.0	0.0
$\beta' a = 0.5$	0.25	0.433	$\beta' a = 0.5$	0.433	0.25
$\beta' a = 1.0$	0.50	0.866	$\beta' a = 1.0$	0.866	0.50
$\beta' a = 1.5$	0.75	1.299	$\beta' a = 1.5$	1.299	0.75
$\beta' a = 2.0$	1.0	1.732	$\beta' a = 2.0$	1.732	1.0

this tendency may become tangled for a large value of the gradient parameter $\beta' a$: the normalized dynamic stress intensity factors $\overline{K}_{\mathrm{III}}^{+}(t)$ and $\overline{K}_{\mathrm{III}}^{-}(t)$ may increase or decrease with increasing gradient parameter $\beta' a$, and a more markable oscillation in the dynamic stress intensity factors is noted in the large-time range. Guided by Fig. 6 for Case II, it is conjectured that the tangled situation, especially the more markable oscillation in the dynamic stress intensity factors, is caused mainly by the material gradient normal to the crack-plane. In spite of this complication, the peak value of the dynamic stress intensity factor $\overline{K}_{\mathrm{III}}^{+}(t)$ increases while the maximum $\overline{K}_{\mathrm{III}}^{-}(t)$ decreases with increasing gradient parameter $\beta' a$.

Finally, the dynamic overshoot of the stress intensity factors for two selected orientation angles $\phi = 30°$ and 60° is given in Table 6 and Fig. 15, versus the gradient parameter $\beta' a$. For $\phi = 60°$, the dynamic overshoot of the stress intensity factor at the crack-tip in the direction of increasing material constants increases, while that at the crack-tip in the direction of decreasing material constants decreases with increasing gradient parameter $\beta' a$. For $\phi = 30°$, the dynamic overshoot of the stress intensity factor at the

Table 6
Dynamic overshoot of the stress intensity factors for $\phi = 30°$ and 60°

$\phi = 30°$	Overshoot K_{III}^{+}	Overshoot K_{III}^{-}	$\phi = 60°$	Overshoot K_{III}^{+}	Overshoot K_{III}^{-}
$\beta' a = 0.0$	26.14%	26.14%	$\beta' a = 0.0$	26.14%	26.14%
$\beta' a = 0.5$	28.94%	23.86%	$\beta' a = 0.5$	33.39%	23.84%
$\beta' a = 1.0$	34.05%	23.48%	$\beta' a = 1.0$	43.60%	22.12%
$\beta' a = 1.5$	42.55%	25.04%	$\beta' a = 1.5$	56.05%	19.81%
$\beta' a = 2.0$	54.21%	27.46%	$\beta' a = 2.0$	70.01%	17.17%

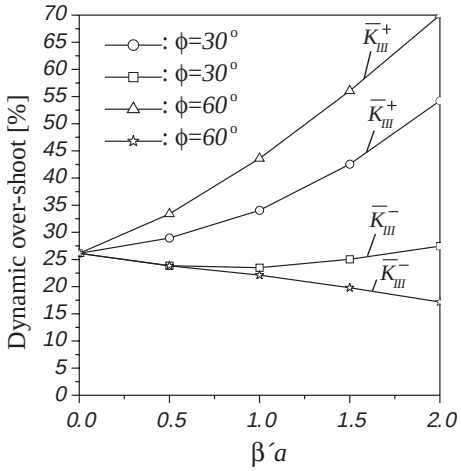

Fig. 15. Dynamic overshoot of the stress intensity factors for Case III ($\phi = 30°$ and 60°).

crack-tip $x_1 = +a$ has a similar behavior as for $\phi = 60°$, while that at the crack-tip $x_1 = -a$ is somewhat complicated. In the latter case, the dynamic overshoot of the stress intensity factor may increase or decrease with increasing gradient parameter $\beta' a$ depending on the magnitude of $\beta' a$.

5. Conclusions

In this paper, transient dynamic crack analysis in a FGM is presented. A hypersingular time-domain traction BIEM is applied for solving the initial-boundary value problem. The spatial variations of the material parameters of the FGM are determined by an exponential law, which is able to describe both the unidirectional and the bidirectional material gradation. Transient dynamic stress intensity factors for a finite crack in an infinite FGM subjected to an impact anti-plane crack-face loading are computed numerically. The present time-domain BIEM has the following special features and advantages:

- It avoids the use of an explicit expression of the time-domain Green's functions, which are not available for general FGM. In lieu of this, the corresponding Laplace-domain Green's functions are required, which can be expressed as Fourier integrals.
- No special regularization or integration techniques are needed for computing the arising hypersingular Hadamard finite-part integral.
- The system matrix is symmetric and only a single spatial integral has to be computed numerically though the application of a spatial Galerkin method.
- It is highly accurate and efficient for computing the transient dynamic stress intensity factors. Extensive numerical tests show that the time-stepping scheme presented here is quite insensitive to the selected time-steps, which is crucial in the conventional time-domain method using time-domain Green's functions.

From the numerical results obtained in this analysis, the following conclusions can be drawn:

- The material gradients in a FGM may have significant influences on the transient dynamic stress intensity factors and their dynamic overshoot over the corresponding static stress intensity factors. This con-

cerns both the peak value or the dynamic overshoot of the dynamic stress intensity factors and the time instant at which the peak value arises.

- For the case with a material gradient parallel to the crack-plane (Case I) and compared to the corresponding values for a homogenous material, the material gradient results in an increase of the peak dynamic stress intensity factor at the crack-tip in the direction of increasing material parameters, while a decrease of the dynamic stress intensity factor at the crack-tip in the direction of decreasing material parameters. The same conclusion also applies for the dynamic overshoot of the stress intensity factors. The dynamic stress intensity factor at the crack-tip in the direction of increasing material parameters is larger than that at the crack-tip in the direction of decreasing material parameters.
- For a material gradient normal to the crack-plane (Case II) and for a small value of the material gradient parameter, the maximum dynamic stress intensity factors increase with increasing material gradient parameter. For a large value of the material gradient parameter, however, a tangled situation and a more pronounced oscillation in the dynamic stress intensity factors is induced. In the latter case, additional local peak dynamic stress intensity factors with slowly decreasing amplitudes are observed. For small gradient parameter, the dynamic overshoot of the stress intensity factors is insensitive to the material gradient, whereas it increases with increasing material gradient for large gradient parameter.
- For material gradients parallel and normal to the crack-plane (Case III) as considered in this analysis for a unidirectional material gradation with an arbitrarily oriented crack, both the crack orientation and the material gradient may have considerable influences on the normalized dynamic stress intensity factors and their dynamic overshoot over the corresponding static stress intensity factors. A maximum dynamic overshoot of the stress intensity factor at the crack-tip in the direction of increasing material constants is obtained for a crack orientation parallel to the direction of the material gradation, i.e., Case I of Fig. 1. However, the corresponding dynamic overshoot of the stress intensity factor at the crack-tip in the direction of decreasing material constants is the lowest in this case. For a crack orientation around 45° with respect to the direction of the material gradient, a tendency combining the effects induced by a material gradient parallel/normal to the crack-plane, i.e., the effects in Cases I and II, is noted.

References

Abramowitz, M., Stegun, I.A., 1972. Handbook of Mathematical Functions. Dover Publications, New York.

Aliabadi, M.H., 2002. The Boundary Element Method, Volume 2, Applications in Solids and Structures. John Wiley & Sons, Inc.

Atkinson, C., 1975. Some results on crack propagation in media with spatially varying elastic moduli. Int. J. Fract. 11, 619–628.

Atkinson, C., List, R.D., 1978. Steady state crack propagation into media with spatially varying elastic properties. Int. J. Eng. Sci. 16, 717–730.

Babaei, R., Lukasiwicz, S.A., 1998. Dynamic response of a crack in a functionally graded material between two dissimilar half planes under antiplane shear impact load. Eng. Fract. Mech. 60, 479–487.

Beskos, D.E., 1997. Boundary element methods in dynamic analysis. Part II (1986–1996). Appl. Mech. Rev. 50, 149–197.

Domínguez, J., 1993. Boundary Elements in Dynamics. Computational Mechanics Publications, Southampton, UK.

Erdogan, F., 1995. Fracture mechanics of functionally graded materials. Compos. Eng. 5, 753–770.

Gradshteyn, I.S., Ryzhik, I.M., 1980. Table of Integrals, Series, and Products. Academic Press, Inc, London.

Li, C., Duan, Z., Zou, Z., 2002. Torsional impact response of a penny-shaped interface crack in bonded materials with a graded material interlayer. ASME J. Appl. Mech. 69, 303–308.

Li, C., Weng, G.J, 2001. Dynamic stress intensity factor of a cylindrical interface crack with a functionally graded interlayer. Mech. Mater. 33, 325–333.

Li, C., Weng, G.J., 2002a. Yoffe-type moving crack in a functionally graded piezoelectric material. Proc. Roy. Soc. Lond. A 458, 381–399.

Li, C., Weng, G.J., 2002b. Dynamic fracture analysis of a penny-shaped crack in a functionally graded material interlayer. Math. Mech. Solids 7, 149–163.

Li, C., Weng, G.J., Duan, Z., 2001a. Dynamic behavior of a cylindrical crack in a functionally graded interlayer under torsional loading. Int. J. Solids Struct. 38, 7473–7485.

Li, C., Weng, G.J., Duan, Z., Zou, Z., 2001b. Dynamic stress intensity factor of a functionally graded material with a finite crack under anti-plane shear loading. Acta Mech. 149, 1–10.

Li, C., Zou, Z., 1999. Torsional impact response of a functionally graded material with a penny-shaped crack. ASME J. Appl. Mech. 62, 566–567.

Li, C., Zou, Z., Duan, Z., 1999. Torsional impact response of a transversely isotropic solid with functionally graded moduli and a penny-shaped crack. Theor. Appl. Fract. Mech. 32, 157–163.

Li, C., Zou, Z., Duan, Z., 2000. Dynamic stress field around the mode III crack tip in an orthotropic functionally graded material. Appl. Math. Mech. 21, 651–658.

Lubich, C., 1988. Convolution quadrature and discretized operational calculus. I. Numer. Math. 52, 129–145.

Marur, P.R., Tippur, H.V., 2000. Dynamic response of bimaterial and graded interface cracks under impact loading. Int. J. Fract. 103, 95–109.

Meguid, S.A., Wang, X.D., Jiang, L.Y., 2002. On the dynamic propagation of a finite crack in functionally graded materials. Eng. Fract. Mech. 69, 1753–1768.

Miyamoto, Y., Kaysser, W.A., Rabin, B.H., Kawasaki, A., Ford, R.G. (Eds.), 1999. Functionally Graded Materials. Kluwer Academic Publishers, Boston.

Nakagaki, M., Sasaki, H., Hagihara, S., 1995. A study of crack in functionally graded material under dynamic loading. ASME PVP 300, 1–6.

Nakagaki, M., Wu, Y.D., Hagihara, S., 1998. Dynamically propagating crack in graded particle dispersed composites. Fracture Strength Solids 145, 333–342.

Parameswaran, V., Shukla, A., 1998. Dynamic fracture of a functionally graded material having discrete property variation. J. Mater. Sci. 33, 3303–3311.

Parameswaran, V., Shukla, A., 1999. Crack-tip stress fields for dynamic fracture in functionally graded materials. Mech. Mater. 31, 579–596.

Rousseau, C.-E., Tippur, H.V., 2001a. Dynamic fracture of compositionally graded materials with cracks along the elastic gradient: experiments and analysis. Mech. Mater. 33, 403–421.

Rousseau, C.-E., Tippur, H.V., 2001b. Influence of elastic gradient profiles on dynamically loaded functionally graded materials: cracks along the gradient. Int. J. Solids Struct. 38, 7839–7856.

Rousseau, C.-E., Tippur, H.V., 2002. Influence of elastic variations on crack initiation in functionally graded glass-filled epoxy. Eng. Fract. Mech. 69, 1679–1693.

Thau, S.A., Lu, T.-H., 1970. Diffraction of transient horizontal shear waves by a finite crack and a finite rigid ribbon. Int. J. Eng. Sci. 8, 857–874.

Wang, B., Han, J., Du, S., 1998. Dynamic fracture mechanics analysis for composite material with material nonhomogeneity in thickness direction. Acta Mech. Solid Sin. 11, 84–93.

Wang, X.D., Meguid, S.A., 1995. On the dynamic crack propagation in an interface with spatially varying elastic properties. Int. J. Fractue 69, 87–99.

Zhang, Ch., 2002. A 2D hypersingular time-domain traction BEM for transient elastodynamic crack analysis. Wave Motion 35, 17–40.

Zhang, Ch., Savaidis, A., Savaidis, G., Zhu, H., 2003. Transient dynamic analysis of a cracked functionally graded material by a BIEM. Comput. Mater. Sci. 26, 167–174.

Zhang, Ch., Savaidis, A., Zhu, H., 2001. A time-domain BIEM for crack analysis in functionally graded materials under impact loading. In: Denda, M. et al. (Eds.), Advances in Boundary Element Techniques II. Hoggar Press, pp. 405–412.